



Satellite-detected sea surface chlorophyll-a blooms in the Japan/East Sea: magnitude and timing

Dingqi Wang^{1,2}, Guohong Fang^{1,3,4}, Shumin Jiang^{1,2}, Qinzeng Xu¹, Guanlin Wang^{1,3,4}, Zexun Wei^{1,3,4}, Yonggang Wang^{1,3,4}, and Tengfei Xu^{1,3,4}

¹ First Institute of Oceanography and Key Laboratory of Marine Science and Numerical Modeling, Ministry of Natural Resources, Qingdao 266061, China

² College of Oceanic and Atmospheric Sciences, Ocean University of China, Qingdao, 266061, China

³ Laboratory for Regional Oceanography and Numerical Modeling, Pilot National Laboratory for Marine Science and Technology, Qingdao 266237, China

⁴ Shandong Key Laboratory of Marine Science and Numerical Modeling, Qingdao 266061, China

Correspondence to: Tengfei Xu (xutengfei@fio.org.cn)

Abstract. The Japan/East Sea (JES) is known as a mid-latitude “Miniature Ocean” that features multiscale oceanic dynamics processes. We investigate the variability of the sea surface chlorophyll-a concentration (SSC) and bloom timing in the JES based on satellite remote sensing products spanning 1998–2019. The JES SSC exhibits strong seasonal variability and blooms twice annually, which are mainly governed by the physical environmental conditions. However, the influences of local oceanic dynamic processes (e.g., upwelling, oceanic fronts, mesoscale eddies, and near-inertial oscillations) on the bloom magnitude and timing of the entire JES are not critical, compared with the PAT and stratification. In addition, significant interannual variabilities of spring bloom magnitude occur along the JES's northwestern coast, and that of fall bloom magnitude occur in the deep Japan Basin. For spring bloom, the interannual variability of the bloom timing (initiation timing, termination timing and duration), which significantly affect the interannual bloom magnitude anomalies, are correlated with climate modes such as AO and ENSO. For fall bloom, on the interannual time scale, the bloom duration is mainly affected by the initiation timing. Both of them have a significant influence on the bloom magnitude. The initiation/termination timing of spring blooms has shifted earlier by 0.37/0.45 days annually along the JES's northwestern coast; the counterpart of fall blooms has shifted 0.49/1.28 days earlier annually in the deep Japan Basin.

Keywords: sea surface chlorophyll-a concentration (SSC); Japan/East Sea (JES); spring bloom; fall bloom; interannual variability

1 Introduction

As the most common primary producer in the marine food chain, phytoplankton respond quickly to changes in their physical environment and are thus sensitive to climate change (Hays et al., 2005). Satellite-based ocean color observations can provide sea surface chlorophyll-a concentrations (SSCs) over the global oceans, which are commonly used for estimating phytoplankton concentrations (Banse, 1977; Liu and Wang, 2022; Taboada et al., 2019; Wang et al., 2021). The Japan/East Sea (JES) is a semi-enclosed marginal sea located in the middle latitudes of the Northwest Pacific Ocean (Fig. 1). The JES involves multi-scale oceanic dynamic processes (Ichiye, 1984), thereby resulting in complicate SSC variations by changing nutrient supply (Park et al., 2020). For instance, the



39 warm Tsushima Current and cold Liman Current forms a thermal boundary in Sea Surface Temperature (SST) in the
40 38–40°N region, namely, a subpolar front (Yamada et al., 2004). The subpolar front induces nutrients accumulation
41 and further favor SSC increases (Lee et al., 2009). Featuring strong offshore monsoons, the JES is abundant with
42 wind-driven Ekman upwelling; this upwelling can carry nutrient-rich water from deeper layers and thus nourish
43 phytoplankton, resulting in heightened SSC (Park et al. 2020). Sea ice-melted water carries high nutrients,
44 promoting the increase of SSCs along the coast of Russia (Martin and Kawase 1998; Nihashi et al., 2017; Park et al.
45 2014). Mesoscale eddies and typhoon also play important roles in SSC variations (Ji et al., 2021; Liu et al., 2019;
46 Maúre et al., 2017). Overall, the upper dynamics in the JES are quite complex, and different processes may
47 counteract with each other in different periods, which leads to the complexities of SSC variations.

48 The phytoplankton concentrations in the JES blooms twice each year, i.e., the spring bloom (March–May) and the
49 fall bloom (October–November), both of which can be detected by satellite observed SSCs (Ishizaka and Yamada,
50 2019; Jo et al., 2014; Kim et al., 2000). Spring blooms, occurring in almost the entire JES, are initiated earlier in the
51 southern region and later in the northern region (Maúre et al., 2017; Yamada et al., 2004). Basically, spring blooms
52 can be explained by the critical depth hypothesis (Sverdrup, 1953). In winter, phytoplankton growth is light-limited
53 (due to deep mixing) rather than being nutrient limited. In spring, the mixed layer becomes shallower than the
54 critical depth, resulting in unlimited light availability to initiate spring bloom (Kim et al., 2000). The critical depth
55 hypothesis is extended by considering the relaxation of turbulent mixing conditions associated with surface cooling
56 (Taylor & Ferrari, 2011) and weakened wind stress (Kim et al., 2007; Lee et al., 2015). Additionally, eddy-driven
57 stratification could regulate the initiation timing of the spring bloom (Mahadevan et al., 2012), with
58 anticyclonic/cyclonic eddy playing different mechanisms, respectively (Maúre et al., 2017). In comparison, fall
59 blooms are much weaker and occur only in the western JES (Kim et al., 2007; Yamada et al., 2004). The fall bloom
60 relies on upward transport of nutrient-rich waters from the deeper layers. It is expected to start when the MLD
61 deepens and becomes equal to the critical depth, as driven by enhanced wind and surface cooling that favor
62 destratification of water column (Kim et al., 2000; Yamada et al., 2004). However, since there are different
63 dynamics and corresponded physical environment factors during spring and fall blooms, it is still a matter of debate
64 about the dominant factors that favor and/or restrict SSC during their bloom and decline stages (Maúre et al., 2017).

65 Additionally, Park et al. (2022) proposed that the interannual variability of SSC is significant in the JES, because
66 the contribution of seasonal cycles to the total variance in SSC variability is less than 30%. Park et al. (2020)
67 suggested that interannual SSC anomalies have only one dominant annual peak that occurs in March or April. The
68 interannual SSC anomaly along the JES's northwestern coast in spring is highly related to the sea ice concentration
69 (SIC) in the Tartar Strait in the previous winter from 1999 to 2007, as more winter SIC would provide more
70 nutrients when melting (Park et al., 2014). For the initial timing, the spring blooms tend to start early/late in El
71 Niño/La Niña years in response to weak/strong wind speed-induced turbulent mixing (Yamada et al., 2004).
72 Meanwhile, the El Niño-Southern Oscillation (ENSO) events can influence the strength and direction of the
73 Tsushima Warm Current to modify the location and maintenance of the subpolar front, which in turn influences the
74 initiation region and timing of the spring bloom (Yoo and Kim, 2004). In comparison, the interannual variability of
75 fall blooms is much weaker, and their initiation timing is less correlated to ENSO-induced wind speed anomalies



over the JES (Yamada et al., 2004). During positive Arctic Oscillation (AO), the SSC anomaly in spring might slightly increase due to the weakening of wind speed and the weak increase of SST in previous winter (Park et al., 2022). However, it is not clear that whether the interannual variability of JES SSC related to climate modes, as the previous research results are based on composite analyses without a test of confidence level.

Furthermore, the temporal variation in bloom magnitude and timing, including initiation timing, termination timing and duration, has significant ecological and biogeochemical influences (Behrenfeld and Boss, 2017). The strong phytoplankton blooms will lead to the imbalance of marine ecosystem, resulting in huge economic losses, especially harmful algal blooms (Ok et al., 2021). Based on observation data from 1972 to 2002, Yamada and Ishizaka (2006) proposed that spring bloom in the southern JES started relatively earlier in mid-1980s, resulting in a regime shift of the community structure of spring diatom from cold water species to warm water species, which are small and adapted to oligotrophic condition. Additionally, in the southern JES, the recruitment of Japanese sardine was positively affected by delays in the start and end timing of the spring bloom, because the overlap of bloom duration and sardine larval periods prolonged (Kodama et al., 2018). However, there is a lack of a study synthesizing variability of bloom magnitude and timing in the seasonal and interannual cycle in the whole JES area. In this study, we attempt to reveal the favorable/restricting factors during the SSC raise and decline stages, and investigate the variations in bloom magnitude and timing in spring and fall, as well as their related physical environmental factors and climate modes, including ENSO and AO.

2 Data and Methods

2.1 Data

The daily SSC data is a Level-4 product providing globally cloud-free estimations during 1998–2019 at a 4-km resolution. The product is published by the Copernicus Marine Environment Monitoring Service (CMEMS), and has merged ocean color observations from multiple sourced satellites (Garnesson et al., 2019). The Level-4 product preserves the information of Level-3 product, and can resolve the SSC variations with time scales longer than intraseasonal (Garnesson et al., 2019; Xu et al., 2021). The *in-situ* chlorophyll-a concentration measurements at 10 m depth obtained from the World Ocean Database 2018 (WOD18), are used to validate the satellite-derived SSC data in the JES (Boyer et al., 2018). A total of 1172 chlorophyll-a profiles during 1998–2019 was obtained (Fig. 1). The satellite-derived SSC data are generally consistent with the *in-situ* observations, with a high correlation coefficient of 0.79 ($p < 0.01$) (Fig. 2). Thus, the satellite-detected SSC data used in this study is reliable for the following research.

The photosynthetically active radiation (PAR) and its attenuation coefficient (k) are provided by the European Service for Ocean Colour with a 4-km horizontal resolution (Maritorena et al., 2010). Satellite-based SIC data in the Tatar Strait (47°–52°N, 139°–142°E) are obtained from the National Snow and Ice Data Center of the National Oceanic and Atmospheric Administration (Meier et al., 2011). The sea surface height (SSH) and sea surface geostrophic current anomalies, with a horizontal resolution of 0.25°×0.25°, are derived from the daily gridded absolute dynamic topography products version 5 and are distributed by the Archiving, Validation, and Interpretation



of Satellite Oceanography (Ducet et al., 2000). Daily SST are derived from the CMEMS with a $0.05^\circ \times 0.05^\circ$ horizontal resolution (Good et al., 2020). The surface wind vector data are provided by the European Centre for Medium-Range Weather Forecasts ERA5 high-resolution reanalysis project, with a horizontal resolution of $0.25^\circ \times 0.25^\circ$ (Hersbach and Dick, 2016). The monthly Niño3.4 and Arctic Oscillation (AO) indices data are collected from the Koninklijk Nederlands Meteorologisch Instituut (KNMI) climate explorer (Trouet et al., 2013). In this study, all data described above cover the period from 1 January 1998 to 31 December 2019. Climatological monthly mean temperature, salinity and nutrient profiles are obtained from the World Ocean Atlas 2018 (WOA18) (Garcia et al., 2019). Details for the datasets used in this study are presented in Table 1.

Table 1. Parameters of the datasets used in this study.

Source	Variables	Temporal Coverage	Temporal resolution	Spatial resolution	URL
CMEMS	SSC	1998–2019	daily	4-km	https://resources.marine.copernicus.eu
WOD18	SSC	1998–2019	-	-	https://www.ncei.noaa.gov/products/world-ocean-database
GlobColour	PAR and k	1998–2019	daily	$0.25^\circ \times 0.25^\circ$	http://www.globcolour.info/
NSIDC	SIC	1998–2019	daily	-	http://nsidc.org/
AVISO	SSH, and sea surface geostrophic current anomalies	1998–2019	daily	$0.25^\circ \times 0.25^\circ$	http://www.aviso.altimetry.fr/duacs/
CMEMS	SST	1998–2019	daily	$0.05^\circ \times 0.05^\circ$	https://resources.marine.copernicus.eu
ERA5	surface wind	1998–2019	6-hourly	$0.25^\circ \times 0.25^\circ$	https://cds.climate.copernicus.eu/cdsapp#!/dataset/reanalysis-era5-single-levels?tab=form
KNMI	Niño3.4, and AO indices	1998–2019	monthly	-	http://climexp.knmi.nl/selectindex.cgi?id=someone@somewhere
WOA18	temperature, salinity and nutrient profiles	-	monthly	$0.25^\circ \times 0.25^\circ$	https://www.ncei.noaa.gov/access/world-ocean-atlas-2018

2.2 Methods

A phytoplankton bloom is defined as a period while the SSC exceeds a certain percentage (20%) of its annual median value over a duration longer than three weeks (spring bloom) or one week (fall bloom), consistent with that used in Maure et al. (2017). As shown in Fig. 3, each grid point has its own threshold SSC value for a bloom. To identify blooms for the entire JES, the threshold SSC value calculated from the area-averaged SSC data is about 0.55 mg m^{-3} .

The Ekman pumping velocity is calculated as follows:



$$w_E = -\nabla \times \left(\frac{\tau}{\rho_0 f} \right)$$

128 where $\rho_0 = 1.025 \times 10^3 \text{ kg/m}^3$, is the mean sea water density, f is the Coriolis parameter, and τ is the wind stress
129 derived from ERA5 wind field product.

130 The eddy kinetic energy (EKE) is calculated as follows

$$EKE = \frac{1}{2}(u'^2 + v'^2)$$

131 where u' and v' are the sea surface geostrophic current anomalies.

132 The wind-induced near-inertial energy flux (WNEF) is estimated by a simple slab mixed layer model as follows
133 (Pollard & Millard, 1970):

$$\Pi(H) = \text{Re}(\mathbf{Z} \cdot \boldsymbol{\tau}^*)$$

134 where $\mathbf{Z} = u + iv$ represents the mixed-layer current, H is the area-averaged climatological monthly mean MLD, and $\boldsymbol{\tau}^*$
135 is the conjugate of $\boldsymbol{\tau}$. A spectral solution through a two-sided Fourier transform is used here, expressed as the
136 following equation:

$$\hat{\mathbf{Z}}(\sigma) = \frac{\hat{\boldsymbol{\tau}}(\sigma)}{H} \frac{r - i(f + \sigma)}{r^2 - i(f + \sigma)^2}$$

137 where $r(\sigma) = r_0(1 - e^{-\sigma^2/2\sigma_c^2})$ is the frequency-dependent damping parameter, σ represents the angular frequency,
138 $r_0 = 0.15f$ and $\sigma_c = f/2$ (Alford, 2003).

139 The Brunt Väisälä frequency, N , is used to estimate the vertical stability in the upper 200 m of the ocean as
140 follows:

$$N = \sqrt{-\frac{g}{\rho} \left(\frac{d\rho}{dz} \right)}$$

141 where g is the gravitational acceleration, ρ is the potential density of sea water, and z is the depth.

142 The MLD is calculated by defining a temperature threshold of 0.3°C from 10 m, as suggested by Jo et al. (2014).
143 Both N and MLD are calculated from the WOA18 data.

144 The gradient-based edge detection algorithm is employed to detect SST fronts (Castelao & Wang, 2014). The
145 monthly frontal probability (FP), which represents the occurrence frequency of SST fronts, is defined as the ratio
146 between the occurrence days of frontal conditions and the total days in the corresponding month.

147 The critical depth (CRD) is computed as follows:

$$CRD = \frac{I_0}{kI_c}$$

148 where I_0 is the PAR ($\text{E m}^{-2} \text{ d}^{-1}$) and k denotes the attenuation coefficient of PAR. The compensation light intensity I_c
149 is taken as $3.8 \text{ E m}^{-2} \text{ d}^{-1}$ (Kim et al., 2000).

150 Principal component analysis (PCA) is a simple, non-parametric method for extracting relevant information from
151 confusing data sets. PCA reduces such datasets to a lower dimension to increase interpretability, but simultaneously
152 preserves as much ‘variability’ (i.e. statistical information) as possible, based on the principle of variance
153 maximization (Jolliffe and Cadima, 2016; Shlens, 2014; Trombetta et al., 2019). Finding new uncorrelated variables,
154 the principal components, reduces to solving an eigenvalue/eigenvector problem, and the new variables are defined



by the dataset at hand, not *a priori*, hence making PCA an adaptive data analysis technique (Jolliffe & Cadima, 2016). This technique is popular for analysis of atmospheric and oceanic data, and is often referred to as Empirical orthogonal function (EOF) called by Lorenz (1956). Both names are commonly used, and the essence of the two is the same. However, EOF often examines the variability in data through space, which is widely used to extract patterns, while PCA is often used to highlight the relationships between different variables over time (Hannachi et al., 2007; Trombetta et al., 2019). In this study, PCA is used to identify the relevant factors that might influence the seasonal SSC cycle following Trombetta et al. (2019), while EOF is employed to explain the spatiotemporal distribution of SSC in the JES on seasonal and interannual time scales (Greene et al., 2019). Prior to the PCA and EOF analysis, the monthly mean SSC data is logarithmically transformed due to its lognormal distribution (Campbell, 1995), as suggested in previous studies (Dandonneau, 1992; Xu et al., 2021).

3 Results

3.1 Seasonal variability of bloom magnitude

The seasonal cycle of the SSC in the JES shows double peaks associated with the bimodal blooms of phytoplankton concentrations in spring and fall, respectively (Fig. 4). The JES SSC is at a low level in boreal winter, with values generally smaller than the threshold SSC value (0.55 mg m^{-3}) used to identify blooms for the entire JES (Fig. 4a–4b). In spring, a bloom occurs around the subpolar front region in March and then extends southward and northward to cover most areas of the JES in April, with SSC values up to 10 mg m^{-3} (Fig. 4c and 4d). In May, SSC begins to decrease from the southeastern JES (Fig. 4e). From June to September, the SSC values are smaller than 0.2 mg m^{-3} in most regions of the JES except for the Tartar Strait (Fig. 4f–4i). Fall bloom begins in October, when the SSCs increase slightly over the entire JES, with smaller magnitudes than spring bloom (Fig. 4j). The SSCs are higher along the Russian and Korean coasts until December (Fig. 4k and 4l).

The seasonal evolution of SSC can be derived by applying EOF analysis on the logarithmic monthly mean SSC (Fig. 5). The first three leading EOF modes explain 64.2%, 8.8% and 3.6% of the total variance. The first EOF mode (EOF1) essentially represents the basin-scale seasonal variability in the JES SSC (Fig. 5). The EOF1 is reminiscent of the SSC distribution in April, showing positive values in the entire JES with relatively small magnitudes in the Japan Basin (Fig. 5a and Fig. 5d). The seasonal time coefficient of EOF1 coincides with the area-averaged SSC in the JES, showing double peaks of 1.36 ± 0.28 and $0.74 \pm 0.07 \text{ mg m}^{-3}$ in April and November, respectively (Fig. 5b). During the December–February and June–September periods, the area-averaged SSC are smaller than the threshold criterion, suggesting poor primary production during these stages.

Previous investigations have qualitatively discussed the potential factors accounting for the seasonal raise and decline in SSC. These factors are summarized as follows (Fig. 6).

(1) PAR (Fig. 6a). In boreal winter, a lower solar altitude angle results in less PAR with an average value of $30.55 \text{ E m}^{-2} \text{ d}^{-1}$. In spring or summer, shortwave radiation increases due to the raise of solar altitude angle.

(2) Nutrient supply (Fig. 6b and 6c). The upper layers of the JES are rich in nutrients during the boreal winter. Both nitrogen and phosphate are rapidly consumed during spring blooms, with the nitrogen concentration decreasing



190 from a peak value of 7.68 in March to 1.06 $\mu\text{mol kg}^{-1}$ in May and the phosphate concentration decreasing from a
191 peak value of 0.58 in March to 0.25 $\mu\text{mol kg}^{-1}$ in May. The nutrients supplementation is poor from June to
192 September when SSC is at a low level, and enhance following October.

193 (3) The MLD and CRD (Fig. 6d). Due to the annual cycle of PAR, the CRD is deepening from January and
194 becomes equal to the shoaling MLD around February, when SSC becomes to increase rapidly. In autumn, SSC
195 reaches the second peak around November when the deepening MLD the shoaling CRD coincides. However, the
196 initiation timing of spring bloom and fall bloom are later than February and earlier than November, respectively.
197 This time bias might be caused by the value of the I_c , as the temporal variations of I_c , of $6.3 \text{ E m}^{-2} \text{ d}^{-1}$ during spring
198 and $1.4 \text{ E m}^{-2} \text{ d}^{-1}$ during fall, is not considered in the calculation of CRD (Kim et al., 2000). Thus, the Sverdrup
199 hypothesis (Sverdrup, 1953) is basically applicable to explain the bloom initiation in the JES, indicating that the
200 variations in the JES SSCs are mainly governed by the physical environmental conditions.

201 (4) The JES shows enhanced stratification from March to August (Fig. 6e) due to weakened wind speeds (Fig. 6f)
202 and strengthened buoyancy fluxes contributed by both surface warming (Fig. 6g) and sea ice melting (Fig. 6h). In
203 contrast, destratification occurs from September until the following February. Stratification is basically out of phase
204 with the MLD; this process can be explained by the fact that strong/weak stratification favors MLD
205 shoaling/deepening. It is worth noting that sea ice melting is also an important nutrient supply source in boreal
206 spring (Park et al., 2014). Since the temporal variations of BV frequency and SST are almost identical, SST is used
207 as the index to quantify stratification in the following analysis.

208 (5) Ocean dynamics contribute to vertical nutrient-water transport (Fig. 6i-6l). Ocean dynamics dominate the
209 upper layer nutrients only in boreal summer and fall, when the upper JES is oligotrophic. After October, nutrients
210 increase in accordance with the enhanced upwelling and frontal probability (Fig. 6i and 6j), and under these
211 processes, deeper nutrient-rich waters are entrained to the upper layer. The EKE shows larger energy in the southern
212 JES from August through December (Fig. 6k). The WNEF shows larger energy in response to the more frequent
213 typhoons in boreal summer and fall (Fig. 6l). However, since mesoscale eddies and typhoon-induced near-inertial
214 oscillations generally occur in the southeastern JES, an area that also has strong stratification, it is suggested that
215 only a few typhoons appreciably increase the nutrient supplies in this area (Iwasaki, 2020). Moreover, the high
216 nutrients induced by WNEF are locally distributed along typhoon tracks and thus do not significantly contribute to
217 the area-averaged nutrients over the entire JES. As a result, the monthly averaged nutrients are not efficiently
218 entrained from the deeper layer to the upper layer to nourish the phytoplankton during the June-September period.
219 Nevertheless, the EKE and WNEF remain at relatively high levels until November; therefore, these factors may still
220 contribute to vertical nutrient transport, albeit they are not critical factors.

221 To identify the dominant and limiting factors affecting the seasonal variability of SSC in the JES, we classify the
222 JES SSC evolution into four stages: the raise stage (January–April) and decline stage (April–July) of spring blooms,
223 and the raise stage (July–November) and decline stage (November–next January) of fall blooms. The relationships
224 between SSC and environmental factors during different stages are examined by PCA analysis (Fig. 7). During the
225 raise stage of spring bloom, the SSC is positively correlated with PAR and negatively correlated with wind speed
226 and SIC, suggesting dominant factors inducing spring blooms include increased PAR, weakened winds and sea ice



melting. In comparison, oceanic dynamics are not correlated with SSC, as revealed by that they are approximately orthogonal to each other. During the decline stage of spring bloom, the stratification shows a symmetrically opposite relationship with SSC, suggesting that SSC decline is related to enhanced stratification. The PAR is saturated and is thereby orthogonal to SSC, and oceanic dynamics are depressed at this time and thus rarely impact SSC. The coincident directions of SSC and FP occur because subpolar fronts are also undergoing a weakening phase at this time (Park et al., 2007). During the raise stage of fall blooms, SSC is positively correlated with the wind speed, upwelling and oceanic fronts; and negatively correlated with PAR and stratification. These results suggest that destratification, strengthening winds and associated upwelling, and enhanced oceanic fronts, favors an increase in SSC by entraining more nutrient-rich waters to the upper layer. The declining PAR tends to play a negative role and acts as a limiting factor for phytoplankton growth when it is reduced to a certain extent. During the decline stage of fall blooms, the winds and associated upwelling tend to enhance the upward transport of nutrient-rich waters to the upper JES. However, limited by decreased PAR and increased sea ice, SSC is still suppressed, resulting in the decay of fall blooms. It is worth noting that the nutrients accumulated during the decline stage of a fall bloom essentially contribute to the following spring bloom.

3.2 Interannual variability of bloom magnitude

The spring and fall blooms are attributed to different mechanisms. Therefore, we conduct EOF analyses for the interannual SSC anomalies (remove seasonal variability) during spring (March–May) and fall (October–November), respectively. EOF1 accounts for 21.2% and 27.0% of the total variances for the spring and fall blooms, respectively. The significant interannual variability of SSC in spring and fall occurs along the JES's northwestern coast (Fig. 8a), and in the deep Japan Basin (Fig. 8b), respectively. The positive spring SSC events occur in 2001, 2002, 2009 and 2016, while negative spring SSC events occur in 2005, 2006, 2012 and 2013 (Fig. 8c). Positive fall SSC events occur in 1999 and 2015, while negative ones occur in 2008 and 2012 (Fig. 8d). Additionally, there is decadal variability in fall blooms, with positive phases during 1998–2002, and 2014–2019, whereas negative phase during 2003–2013.

The interannual variability of JES SSC is positively correlated with PAR, with correlation coefficient (R) of 0.37 at a confidence level of $p < 0.1$ in spring and of $R = 0.12$, $p > 0.1$ in fall (Fig. 9a and 9c). For stratification anomalies, the correlations are $R = 0.55$, $p < 0.01$ in spring and $R = -0.44$, $p < 0.05$ in fall (Fig. 9b and 9d). These correlations suggest that photosynthetic activity positively contributes to the interannual SSC variability in the JES in spring. Meanwhile, strong stratification favors positive SSC anomalies in spring, as explained by the critical depth hypothesis. In contrast, PAR anomalies are not significantly correlated with SSC anomalies in fall, whereas stratification shows a significant negative correlation, suggesting that stronger stratification leads to smaller SSCs by inhibiting the upward transport of nutrient-rich waters to the mixed layer.

By comparing Fig. 10a and 10b, the interannual variability of JES SSC is more statistically correlated with AO ($R = 0.38$, $p < 0.1$) than ENSO ($R = 0.26$, $p > 0.1$) in spring. This correlations suggest that the spring bloom magnitude would increase during positive AO, which demonstrates the previous research results (Park et al., 2022). However,



the climate modes have little effect on modulating the interannual variability of fall bloom magnitude, with low correlation coefficients that far lower than the 90% confidence level, as shown in Fig. 10c and 10d.

3.3 Bloom timing

Spring bloom initiates in the southern and southeastern JES in February–March and in the northwestern JES in April, in agreement with previous investigations (Fig. 11a). Fall blooms initiates in the Tsushima Basin and along the JES coasts from September to early October and in the central basin of the JES from late October to early November (Fig. 11b). Spring blooms are terminated generally in the southwestern JES on 11 April \pm 9 days and subsequently in the northeastern JES on 29 May \pm 9 days (Fig. 11c). Fall blooms generally terminate on 29 November \pm 12 as a result of the rapidly decreasing PAR beginning in late November (Fig. 11d).

Fig. 12 shows the initiation and termination timing of spring blooms along the JES's northwestern coast during 1998–2019. Spring blooms were initiated earlier in 2002, 2010, 2011 and 2014 and later in 1999, 2005, 2006, and 2013; and were terminated earlier in 2002, 2003, 2010 and 2011 and later in 1999, 2000, 2003, and 2006, identified by a threshold value of one standard deviation beyond the climatological mean initiation/termination timing (Fig. 12a). The interannual variability in initiation timing is jointly controlled by PAR, stratification, and sea ice melting, i.e., higher PAR, stronger stratification, and earlier sea ice melting are favorable for earlier spring blooms (Fig. 12b-d)). The termination and initiation timing of fall blooms are significantly correlated, with a correlation coefficient of 0.74 ($p < 0.01$), suggesting that the consumption of upper-layer nutrients determines spring bloom termination, as supplementary nutrients are rarely available from deeper layers. Additionally, the initiation/termination timings show trends of occurring earlier by 0.37/0.45 days per year during 1998–2019, coinciding with the increasing trends in PAR and stratification identified in March and April.

Fall blooms were initiated earlier in 1999, 2015, and 2019, in accordance with strong winds and weak stratification; and were initiated later in 2003, 2006, 2008 and 2010, when weak winds and strong stratification occurred. The fall blooms were terminated early in 2011, 2012, 2017 and 2018 and late in 1998, 1999, 2000, and 2015 (Fig. 13a). In comparison to the significant positive correlation observed between the termination and initiation timing of spring blooms, the corresponding correlation coefficient of fall blooms is only 0.21 ($p > 0.1$). In addition, the initiation/termination timing show trends of occurring earlier by 0.49/1.28 days per year during 1998–2019, which may be related to the intensified/weakened wind speeds during the fall bloom development/decay periods, respectively (Fig. 13b).

As shown in Fig. 14a, for spring bloom along the JES's northwestern coast, the termination timing anomalies are positively correlated with the initiation timing anomalies ($R = 0.75$, $p < 0.01$), while duration anomalies are negatively correlated with the initiation timing anomalies ($R = -0.72$, $p < 0.01$). The correlations show that the SSC anomalies from March to May are negatively correlate with initiation ($R = -0.50$, $p < 0.05$) and termination ($R = -0.55$, $p < 0.01$) timing anomalies, but not statistically correlated with duration anomalies ($R = 0.16$, $p > 0.1$). In comparison, the impact of AO is more important than that of ENSO for spring bloom timing on the interannual time scale, because the spring blooms along the JES's northwestern coast would occur earlier ($R = -0.47$, $p < 0.05$) and be more prolonged ($R = 0.37$, $p < 0.1$) during positive AO, and would terminate earlier during El Niño events ($R = -$



0.42, $p < 0.1$). For fall bloom in the deep Japan Basin, duration anomalies are mainly affected by the initiation timing anomalies with a negative correlation coefficient of -0.57 above 99% confidence level (Fig. 14b). In addition, on interannual time scale, the bloom magnitude is negatively correlated with the initiation timing with a value of -0.73 ($p < 0.01$), and positively correlated with bloom duration with a value of 0.78 ($p < 0.01$). Furthermore, the climate modes also have little effect on modulating the interannual variability of fall bloom timing.

4 Discussion

The JES is known as a mid-latitude “Miniature Ocean” in which multiscale oceanic dynamical processes (e.g., cross-basin warm and cold currents, upwelling, oceanic fronts, mesoscale eddies, and near-inertial oscillations) and sea ice occur. The marine ecosystems of the JES are influenced by these complicated processes. The phytoplankton concentrations can be evidenced by the SSC variability. Previous investigations have revealed bimodal phytoplankton concentrations blooms occurring in spring and fall. These blooms can be explained by the critical depth hypothesis, which emphasizes the roles of sea surface wind speeds and temperatures (Chiswell et al. 2013; Kim et al., 2000; Kim et al. 2007; Taylor and Ferrari, 2011; Yamada et al., 2004). In this study, we revisit the spring and fall phytoplankton blooms and their mechanisms based on a newly released high-resolution satellite-derived SSC product.

On interannual time scale, the bloom magnitude anomaly is not statistically correlated with bloom duration anomaly in spring. This lack of correlation can be attributed to different control factors affecting the durations and magnitudes of spring blooms. There is adequate light in the entire JES during the spring bloom period, while strong stratification prevents the upward transport of deep, nutrient-rich waters to supply the upper layer. Therefore, the bloom duration is mainly controlled by the consumption rate of the accumulated nutrients in the upper layer. SSCC is a phytoplankton biomass indicator that is related to the amount of accumulated nutrients. Both the phytoplankton biomass and the bloom duration are positively correlated with the accumulated nutrients. However, more phytoplankton biomass leads to faster nutrient consumption. Thus, this relation tends to result in a negative correlation between the durations of and SSCC anomalies associated with spring blooms. As a result, no significant correlation is found between the spring bloom durations and SSCC anomalies.

However, for fall bloom, the interannual variability of bloom magnitude is significantly correlated with the interannual variability of bloom duration. In comparison with spring bloom, nutrients are limited during the fall bloom period. The growth of phytoplankton biomass depends on the nutrients supplied by the vertical transport of deep waters through dynamic oceanic processes. Moreover, these nutrients are consumed immediately after being transported to the upper layer, and thus, the consumption rate of the nutrients can be ignored. Persistent and active oceanic dynamic processes tend to transport more nutrient-rich waters to the upper layer, favoring both increased SSCCs and prolonged fall bloom durations.

Relative to the AO, The interannual bloom magnitude and timing anomalies in the JES are not statistically correlated with the ENSO, although some existing studies have suggested that El Niño events favor earlier spring blooms by comparing SSCs recorded in typical El Niño years (e.g., 1998 and 2002) with those representing normal or La Niña years (e.g., 1999 and 2001) (Yamada et al., 2004; Yoo and Kim, 2004). Indeed, the JES is influenced by



334 ENSO at interannual time scales (Cheon, 2020; He et al., 2017; Son et al. 2016; Wang and Chan 2002; Wang et al.
335 2000). However, ENSO event-induced anomalies somehow result in contradictory SSC responses in the JES. For
336 instance, El Niño events tend to be followed by weak wind speeds that favor early spring blooms (Yamada et al.,
337 2004). On the other hand, El Niño events tend to co-occur with warm winters and thus less sea ice, thus favoring
338 negative spring SSC anomalies in the JES (Hong et al., 2001; Park et al., 2014). In terms of fall blooms, higher
339 SSCs and longer bloom durations are expected, as active typhoons benefit the vertical transport of nutrient-rich
340 waters during El Niño years (Goh and Chan, 2010). However, at the same time, the warmer background states that
341 occur during the summer-fall seasons in the JES act to inhibit SSC increases and thus cancel out the role of typhoons
342 (Cheon, 2020).

343 However, some issues remain unclear, including but not limited to (1) obtaining a quantitative assessment of the
344 driving factors that account for JES SSC variabilities; (2) the relation between JES SSCs and climate change; and (3)
345 the JES SSC variabilities induced by changes in the phytoplankton community structure and the interactions
346 between grazers and phytoplankton. Especially, the complex predator-prey interactions are crucial to the temporal
347 changes in phytoplankton concentrations (Behrenfeld, 2010; Behrenfeld and Boss, 2017). Thus, these pending issues
348 must be further investigated through interdisciplinary collaboration.

349 **5 Summary**

350 In this study, we investigate the spring and fall SSC blooms and their interannual variability by employing high-
351 resolution satellite remote sensing products. The new findings are summarized as follows.

352 (1) On the annual cycle, the influences of local oceanic dynamic processes (e.g., upwelling, oceanic fronts,
353 mesoscale eddies, and near-inertial oscillations) on the bloom magnitude and timing of the entire JES are limited,
354 compared with the PAT and stratification.

355 (2) The interannual variability in the JES SSC consists of spring and fall components, which occur along the
356 JES's northwestern coast and in the deep JES basin, respectively. Stronger PAR and stratification favor positive SSC
357 anomalies of spring bloom, whereas weaker stratification favors positive SSC anomalies of fall bloom.

358 (3) For spring bloom, the interannual variations in initiation timing have crucial effect on the interannual
359 variations in termination timing, duration and magnitude. However, the interannual variability of bloom magnitude
360 is not statistically correlated with that of bloom duration. Additionally, during positive AO, the bloom magnitude
361 would increase, and spring blooms along the JES's northwestern coast would occur early and be prolonged. During
362 El Niño events, spring blooms tend to terminate early. The spring bloom initiation/termination timing has shifted
363 earlier by 0.37/0.45 days annually along the JES's northwestern coast.

364 (4) For fall bloom, duration anomalies are mainly affected by the initiation timing anomalies with a negative
365 correlation coefficient of -0.57. Moreover, the bloom magnitude is significantly correlated with the initiation timing
366 bloom duration on interannual time scale. However, the climate modes also have little effect on modulating the
367 interannual variability of fall bloom timing, since fall blooms are dominated by oceanic dynamic processes. The fall
368 blooms initiation/termination timing has shifted 0.49/1.28 days earlier annually in the deep Japan Basin.



369 (5) Relative to the AO, the interannual variability in JES SSCs are not statistically correlated with ENSO, which
370 tends to induce atmospheric and/or oceanic anomalies that favor a counterbalanced response in SSC.

371 *Code and data availability.* The SSC data are available at <https://resources.marine.copernicus.eu>. The *in situ*
372 chlorophyll-a concentration data are available at <https://www.ncei.noaa.gov/products/world-ocean-database>. The
373 PAR and *k* data are available at <http://www.globcolour.info/>. The SIC data are available at <http://nsidc.org/>. The
374 SSH and sea surface geostrophic current anomalies data are available at <http://www.aviso.altimetry.fr/duacs>. The
375 SST data are <https://resources.marine.copernicus.eu>. The surface wind vectore data are available at
376 <https://cds.climate.copernicus.eu/cdsapp#!/dataset/reanalysis-era5-single-levels?tab=form>. The monthly Niño3.4 and
377 AO indices are available at <http://climexp.knmi.nl/selectindex.cgi?id=someone@somewhere>. The WOA18 data are
378 available at <https://www.ncei.noaa.gov/access/world-ocean-atlas-2018>.

379

380 *Author contributions.* **Dingqi Wang:** Writing – original draft, Writing – review & editing, Methodology, Software.
381 **Guohong Fang:** Writing – review & editing, Supervision. **Shumin Jiang:** Writing – original draft, Methodology.
382 **Qinzeng Xu:** Writing – review & editing. **Guanlin Wang:** Writing – review & editing. **Zexun Wei:** Writing – review
383 & editing, Funding acquisition. **Yonggang Wang:** Writing – review & editing. **Tengfei Xu:** Writing – review &
384 editing, Resources, Funding acquisition.

385

386 *Competing interests.* The contact author has declared that neither they nor their co-author has any competing
387 interests.

388

389 *Disclaimer.* Publisher's note: Copernicus Publications remains neutral with regard to jurisdictional claims in
390 published maps and institutional affiliations.

391

392 *Financial support.* This study is jointly supported by the National Key Research and Development Program of
393 China (Grant No. 2020YFA0608800), and the National Natural Science Foundation of China (Grant No. 41821004).
394 This work got the data service support from the Marine Environment Data Service System which supported by the
395 National Key Research and Development Program of China (2019YFC1408405).

396 References

- 397 Alford, M. H.: Improved global maps and 54-year history of wind-work on ocean inertial motions, *Geophysical*
398 *Research Letters*, 30 (8), 1424, <https://doi.org/10.1029/2002GL016614>, 2003.
- 399 Banse, K.: Determining the carbon-to-chlorophyll ratio of natural phytoplankton, *Marine Biology*, 41, 199–212,
400 <https://doi.org/10.1007/BF00394907>, 1977.
- 401 Behrfield, M. J.: Abandoning Sverdrup's Critical Depth Hypothesis on phytoplankton blooms, *Ecology*, 91 (4),
402 977–989, <https://doi.org/10.1890/09-1207.1>, 2010.
- 403 Behrfield, M. J. and Boss, E. S.: Student's tutorial on bloom hypotheses in the context of phytoplankton annual
404 cycles, *Global Change Biology*, 24 (1), 55–77, <https://doi.org/10.1111/gcb.13858>, 2017.



- 405 Boyer, T. P., Baranova O. K., Coleman, C., Garcia, H. E. , Grodsky, A., Locarnini, R. A., Mishonov, A. V., Paver, C.
406 R., Reagan, J. R., Seidov, D., Smolyar, I. V., Weathers, K., and Zweng, M. M.: World Ocean Database
407 2018: A.V. Mishonov, Technical Ed., NOAA Atlas NESDIS 87, 2018.
- 408 Campbell, J. W.: The lognormal distribution as a model for bio-optical variability in the sea, *Journal of Geophysical*
409 *Research*, 100 (7), 13,237–13,254, <https://doi.org/10.1029/95JC00458>, 1995.
- 410 Castelao, R. M. and Wang, Y.: Wind-driven variability in sea surface temperature front distribution in the California
411 Current System, *J. Geophys. Res. Oceans*, 119 (3), 1861–1875, <https://doi.org/10.1002/2013JC009531>,
412 2014.
- 413 Cheon, W. G.: The Summer/Fall Variability of the Southern East/Japan Sea in the ENSO Period, *Ocean Science*
414 *Journal*, 55, 341–352, <https://doi.org/10.1007/s12601-020-0027-5>, 2020.
- 415 Chiswell, S. M., Bradford-Grieve, J., Hadfield, M. G., and Kennan, S. C.: Climatology of surface chlorophyll a,
416 autumn-winter and spring blooms in the southwest Pacific Ocean, *Journal of Geophysical Research*,
417 *Oceans*, 118, 1003–1018. <https://doi.org/10.1002/jgrc.20088>, 2013.
- 418 Dandonneau, Y.: Surface chlorophyll concentration in the tropical Pacific Ocean: an analysis of data collected by
419 merchant ships from 1978 to 1989, *Journal of Geophysical Research*, 97 (C3), 3581–3591,
420 <https://doi.org/10.1029/91JC02848>, 1992.
- 421 Ducet, N., Le, Traon, P. Y., and Reverdin, G.: Global high-resolution mapping of ocean circulation from
422 TOPEX/Poseidon and ERS-1 and-2, *Journal of Geophysical Research, Oceans* 105 (C8), 19477–19498,
423 <https://doi.org/10.1029/2000JC900063>, 2000.
- 424 Garcia, H. E., Boyer, T. P., Baranova, O. K., Locarnini, R. A., Mishonov, A. V., Grodsky, A., Paver, C. R.,
425 Weathers, K. W., Smolyar, I. V., Reagan, J. R., Seidov, D., and Zweng, M. M.: World Ocean Atlas 2018:
426 Product Documentation. A. Mishonov, Technical Editor, 2019.
- 427 Garnesson, P., Mangin, A., D'Andon, O. F., Demaria, J., and Bretagnon, M.: The CMEMS GlobColour chlorophyll
428 a product based on satellite observation: multi-sensor merging and flagging strategies, *Ocean Science*, 15,
429 819–830, <https://doi.org/10.5194/os-15-819-2019>, 2019.
- 430 Goh, A. Z. and Chan, J. C. L.: Variations and prediction of the annual number of tropical cyclones affecting Korea
431 and Japan, *International Journal of Climatology*, 32 (2), 178–189, <https://doi.org/10.1002/joc.2258>, 2010.
- 432 Gong, D., Wang, S., and Zhu, J.: East Asian winter monsoon and Arctic Oscillation, *Geophysical Research Letters*,
433 28 (10), 2073–2076, <https://doi.org/10.1029/2000GL012311>, 2001.
- 434 Good, S., Fiedler, E., Mao, C., Martin, M. J., Maycock, A., Reid, R., Roberts-Jones, J., Searle, T., Waters, J., While,
435 J., and Worsfold, M.: The Current Configuration of the OSTIA System for Operational Production of
436 Foundation Sea Surface Temperature and Ice Concentration Analyses. *Remote Sensing*, 12, 720,
437 <https://doi.org/10.3390/rs12040720>, 2020.
- 438 Greene, C. A., Thirumalai, K., Kearney, K. A., Delgado, J. M., Schwanghart, W., Wolfenbarger, N. S., Thyng, K.
439 M., Gwyther, D. E., Gardner A. S., and Blankenship, D. D.: The Climate Data Toolbox for MATLAB,
440 *Geochem. Geophysics Geosystems*, 20, <https://doi.org/10.1029/2019GC008392>, 2019.



- 441 Hannachi, A., Jolliffe, I. T., and Stephenson, D. B.: Empirical orthogonal functions and related techniques in
442 atmospheric science: A review, *International Journal of Climatology*, 27 (9), 1119–1152,
443 <https://doi.org/10.1002/joc.1499>, 2007.
- 444 Hays, G., Richardson, A., and Robinson, C.: Climate change and marine plankton, *Trends in Ecology and Evolution*
445 20 (6), 337–344, <https://doi.org/10.1016/j.tree.2005.03.004>, 2005.
- 446 He, S., Gao, Y., Li, F., Wang, H., and He, Y.: Impact of Arctic Oscillation on the East Asian climate: A review,
447 *Earth-Science Reviews*, 164, 48–62, <https://doi.org/10.1016/j.earscirev.2016.10.014>, 2017.
- 448 Hersbach, H. and Dick, D.: ERA5 reanalysis is in production, *ECMWF Newsletter*, 147, 2016.
- 449 Hong, C., Cho, K., and Kim, H.: The relationship between ENSO events and sea surface temperature in the East
450 (Japan) Sea, *Progress in Oceanography*, 49, 21–40, [https://doi.org/10.1016/S0079-6611\(01\)00014-3](https://doi.org/10.1016/S0079-6611(01)00014-3), 2001.
- 451 Ichiye, T.: Some problems of circulation and hydrography of the Japan Sea and the Tsushima Current, Elsevier
452 *Oceanography Series*, 39, 15–54, [https://doi.org/10.1016/S0422-9894\(08\)70289-7](https://doi.org/10.1016/S0422-9894(08)70289-7), 1984.
- 453 Ishizaka, J. and Yamada, K.: Phytoplankton and primary production in the Japan Sea. In: Barale, V. and Gade, M
454 (eds.): *Remote Sensing of the Asian Seas*, Springer, Cham, 177–189, [https://doi.org/10.1007/978-3-319-](https://doi.org/10.1007/978-3-319-94067-0_9)
455 [94067-0_9](https://doi.org/10.1007/978-3-319-94067-0_9), 2019.
- 456 Ji, C., Zhang, Y., Cheng, Q., and Tsou, J. Y.: Investigating ocean surface responses to typhoons using reconstructed
457 satellite data, *International Journal of Applied Earth Observation and Geoinformation*, 103, 102474,
458 <https://doi.org/10.1016/j.jag.2021.102474>, 2021.
- 459 Jo, C. O., Park, S., Kim, Y. H., Park, K., Park, J. J., Park, M., Li, S., Kim, J., Park, J., Kim, J., and Kim, K.: Spatial
460 distribution of seasonality of SeaWiFS chlorophyll-a concentrations in the East/Japan Sea, *Journal of*
461 *Marine Systems*, 139, 288–298, <https://doi.org/10.1016/j.jmarsys.2014.07.004>, 2014.
- 462 Jolliffe, I. T. and Cadima, J.: Principal component analysis: a review and recent developments, *Phil. Trans. R. Soc.*
463 *A*, 374, 20150202, <http://dx.doi.org/10.1098/rsta.2015.0202>, 2016.
- 464 Kim, H., Yoo, S., and Oh, I. S.: Relationship between phytoplankton bloom and wind stress in the sub-polar frontal
465 area of the Japan/East Sea. *Journal of Marine Systems*, 67, 205–216.
466 <https://doi.org/10.1016/j.jmarsys.2006.05.016>, 2007.
- 467 Kim, S., Saitoh, S., Ishizaka, J., Isoda, Y., and Kishino, M.: Temporal and Spatial Variability of Phytoplankton
468 Pigment Concentrations in the Japan Sea Derived from CZCS Images, *Journal of Oceanography*, 56, 527–
469 538, <https://doi.org/10.1023/A:1011148910779>, 2000.
- 470 Kodama, T., Wagawa, T., Ohshimo, S., Morimoto, H., Iguchi, N., Fukudome, K., Goto, T., Takahashi, M., Yasuda,
471 T.: Improvement in recruitment of Japanese sardine with delays of the spring phytoplankton bloom in the
472 Sea of Japan, *Fisheries Oceanography*, 27, 289–301, <https://doi.org/10.1111/fog.12252>, 2018.
- 473 Lee, J., Kang, D., Kim, I., Rho, T., Lee, T., Kang, C., and Kim, K.: Spatial and temporal variability in the pelagic
474 ecosystem of the East Sea (Sea of Japan): A review, *Journal of Marine Systems*, 78 (2), 288–300,
475 <https://doi.org/10.1016/j.jmarsys.2009.02.013>, 2009.



- 476 Lee, S., Yoo, S., and Son Y. B. Variability of chlorophyll-a bloom timing associated with physical forcing in the
477 East Sea/Sea of Japan (1998–2014). PICES-2015 Annual Meeting, Qingdao.
478 <https://meetings.pices.int/publications/book-of-abstracts/2015-PICES-Book-of-Abstracts.pdf>, 2015.
- 479 Liu, X. and Wang, M.: Global daily gap-free ocean color products from multi-satellite measurements, International
480 Journal of Applied Earth Observation and Geoinformation, 108, 102714,
481 <https://doi.org/10.1016/j.jag.2022.102714>, 2022
- 482 Liu, Y., Tang, D., and Evgeny, M.: Chlorophyll Concentration Response to the Typhoon Wind-Pump Induced
483 Upper Ocean Processes Considering Air-Sea Heat Exchange, Remote Sensing, 11, 1825,
484 <https://doi.org/10.3390/rs11151825>, 2019.
- 485 Lorenz, E. N.: Empirical Orthogonal Functions and Statistical Weather Prediction, Scientific Report, 1, Statistical
486 Forecasting Project, Department of Meteorology, MIT, Cambridge, 1956.
- 487 Mahadevan, A., D'Asaro, E., Lee, C., and Perry, M. J.: Eddy-driven stratification initiates North Atlantic spring
488 phytoplankton blooms, Science, 337, 54–58, <https://doi.org/10.1126/science.1218740>, 2012.
- 489 Maritorena, S., O., D'Andon, H.F., Mangin, A., and Siegel, D. A.: Merged satellite ocean color data products using a
490 bio-optical model: characteristics, benefits and issues, Remote Sensing of Environment, 114, 1791–1804,
491 <https://doi.org/10.1016/j.rse.2010.04.002>, 2010.
- 492 Martin, S. and Kawase, M.: The southern flux of sea ice in the Tatarskiy Strait, Japan Sea and the generation of the
493 Liman Current, Journal of Marine Research, 56, 141–155, <https://doi.org/10.1357/002224098321836145>,
494 1998.
- 495 Maúre, E. R., Ishizka, J., Sukigara, C., Mino, Y., Aiki, H., Mastsumo, T., Tomita, H., Goes, J. I., and Gomes, H. R.:
496 Mesoscale Eddies Control the Timing of Spring Phytoplankton Blooms: A Case Study in the Japan Sea,
497 Geophysical Research Letters, 44, 11115–11124, <https://doi.org/10.1002/2017GL074359>, 2017.
- 498 Meier, W. N., Savoie, M. H., and Mallory, S.: CDR Climate Algorithm and Theoretical Basis Document: Passive
499 Microwave Sea Ice Concentration. NOAA's NCDC CDR Program, CDRPATBD-0107, Asheville, North
500 Carolina, USA, 2011.
- 501 Nihashi, S., Ohshima, K. I., and Saitoh, S.: Sea-ice production in the northern Japan Sea, Deep-Sea Research Part I,
502 127, 65–76, <http://dx.doi.org/10.1016/j.dsr.2017.08.003>, 2017.
- 503 Ok, J. H., Jeong, H. J., You, J. H., Kang, H. C., Park, S. A., Lim, A. S., Lee, S. Y., and Eom, S. H.: Phytoplankton
504 Bloom Dynamics in Incubated Natural Seawater: Predicting Bloom Magnitude and Timing, Frontiers in
505 Marine Science. 8, 681252, <http://dx.doi.org/10.3389/fmars.2021.681252>, 2021.
- 506 Park, J., Park, K., Kang, C., and Kim G.: Satellite-Observed Chlorophyll-a Concentration Variability and Its Relation
507 to Physical Environmental Changes in the East Sea (Japan Sea) from 2003 to 2015, Estuaries and Coasts,
508 43, 630–645, <https://doi.org/10.1007/s12237-019-00671-6>, 2020.
- 509 Park, K., Park, J., and Kang, C.: Satellite-Observed Chlorophyll-a Concentration Variability in the East Sea (Japan
510 Sea): Seasonal Cycle, Long-Term Trend, and Response to Climate Index, Frontiers in Marine Science, 9,
511 807570, <https://doi.org/10.3389/fmars.2022.807570>, 2022.



- 512 Park, K., Kang, C., Kim, K., and Park, J.: Role of sea ice on satellite-observed chlorophyll-a concentration
513 variations during spring bloom in the East/Japan sea, *Deep-Sea Research I*, 83, 34–44,
514 <https://doi.org/10.1016/j.dsr.2013.09.002>, 2014.
- 515 Park, K., Ullman, D.S., Kim, K., Chung, J. Y., and Kim, K.: Spatial and temporal variability of satellite-observed
516 Subpolar Front in the East/Japan Sea, *Deep Sea Research Part I: Oceanographic Research Papers*, 54 (4),
517 453–470, <https://doi.org/10.1016/j.dsr.2006.12.010>, 2007.
- 518 Pollard, R. T. and Millard, R. C.: Comparison between observed and simulated wind-generated inertial oscillations,
519 *Deep Sea Research and Oceanographic Abstracts*, 17 (4), 813–821, [https://doi.org/10.1016/0011-](https://doi.org/10.1016/0011-7471(70)90043-4)
520 [7471\(70\)90043-4](https://doi.org/10.1016/0011-7471(70)90043-4), 1970.
- 521 Shlens, J.: A tutorial on Principal Component Analysis, *ArXiv*, abs/1404.1100, 2014.
- 522 Son, H., Park, J., and Kug, J.: Precipitation variability in September over the Korean Peninsula during ENSO
523 developing phase, *Climate Dynamics*, 46, 3419–3430, <https://doi.org/10.1007/s00382-015-2776-x>, 2016.
- 524 Sverdrup, H. U.: On conditions for the vernal blooming of phytoplankton, *ICES Journal of Marine Science*, 18 (3),
525 287–295, <https://doi.org/10.1093/icesjms/18.3.287>, 1953.
- 526 Taboada, F. G., Barton, A. D., Stock, C. A., Dunne, J., and John, J. G.: Seasonal to interannual predictability of
527 oceanic net primary production inferred from satellite observations, *Progress in Oceanography*, 170, 28–39,
528 <https://doi.org/10.1016/j.pocean.2018.10.010>, 2019.
- 529 Taylor, J. and Ferrari, R.: Shutdown of turbulent convection as a new criterion for the onset of spring phytoplankton
530 blooms, *Limnology and Oceanography*, 56 (6), 2293–2307, <https://doi.org/10.4319/lo.2011.56.6.2293>,
531 2011.
- 532 Trombetta, T., Vidussi, F., Mas, S., Parin, D., Simier, M., and Mostajir, B.: Water temperature drives phytoplankton
533 blooms in coastal waters. *PLoS ONE* 14 (4), e0214933. <https://doi.org/10.1371/journal.pone.0214933>,
534 2019.
- 535 Trouet, V. and Van Oldenborgh, G. J.: KNMI Climate Explorer: A Web-Based Research Tool for High-Resolution
536 Paleoclimatology, *Tree-Ring Research*, 69, 3–13, <https://doi.org/10.3959/1536-1098-69.1.3>, 2013.
- 537 Wang, B. and Chan, J. C. L.: How Strong ENSO Events Affect Tropical Storm Activity over the Western North
538 Pacific, *Journal of Climate*, 15, 1643–1658, [https://doi.org/10.1175/1520-](https://doi.org/10.1175/1520-0442(2002)015<1643:HSEEAT>2.0.CO;2)
539 [0442\(2002\)015<1643:HSEEAT>2.0.CO;2](https://doi.org/10.1175/1520-0442(2002)015<1643:HSEEAT>2.0.CO;2), 2002.
- 540 Wang, B., Wu, R., and Fu, X.: Pacific-east Asian teleconnection: How does ENSO affect east Asian climate?
541 *Journal of Climate*, 13 (9), 1517–1536, [https://doi.org/10.1175/1520-](https://doi.org/10.1175/1520-0442(2000)013<1517:PEATHD>2.0.CO;2)
542 [0442\(2000\)013<1517:PEATHD>2.0.CO;2](https://doi.org/10.1175/1520-0442(2000)013<1517:PEATHD>2.0.CO;2), 2000.
- 543 Wang, M., Jiang, L., Mikelsons, K., and Liu, X.: Satellite-derived global chlorophyll-a anomaly products,
544 *International Journal of Applied Earth Observation and Geoinformation*, 97, 102288,
545 <https://doi.org/10.1016/j.jag.2020.102288>, 2021.
- 546 Wu, B. and Wang, J.: Winter Arctic Oscillation, Siberian high and East Asian winter monsoon, *Geophysical*
547 *Research Letters*, 29 (19), 1897, <https://doi.org/10.1029/2002GL015373>, 2002.



- 548 Xu, T., Wei, Z., Li, S., Susanto, R. D., Radiarta, N., Yuan, C., Setiawan, A., Kuswardani, A., Agustadi, T., and
549 Trenggono, M.: Satellite-Observed Multi-Scale Variability of Sea Surface Chlorophyll-a Concentration
550 along the South Coast of the Sumatra-Java Islands, Remote Sensing, 13, 2817,
551 <https://doi.org/10.3390/rs13142817>, 2021.
- 552 Yabe, I., Kawaguchi, Y., Wagawa, T., Fujio, S.: Anatomical study of Tsushima Warm Current system:
553 Determination of Principal Pathways and its Variation, Progress in Oceanography, 194, 102590,
554 <https://doi.org/10.1016/j.pocean.2021.102590>, 2021.
- 555 Yamada, K. and Ishizaka, J.: Estimation of interdecadal change of spring bloom timing, in the case of the Japan Sea,
556 Geophysical Research Letters, 33, L02608, <https://doi.org/10.1029/2005GL024792>, 2006.
- 557 Yamada, K., Ishizaka, J., Yoo, S., Kim, H., and Chiba, S.: Seasonal and interannual variability of sea surface
558 chlorophyll a concentration in the Japan/East Sea (JES), Progress in Oceanography, 61, 193–211,
559 <https://doi.org/10.1016/j.pocean.2004.06.001>, 2004.
- 560 Yoo, S. and Kim, H.: Suppression and enhancement of the spring bloom in the southwestern East Sea/Japan Sea,
561 Deep-Sea Research II, 51, 1093–1111, <https://doi.org/10.1016/j.dsr2.2003.10.008>, 2004.

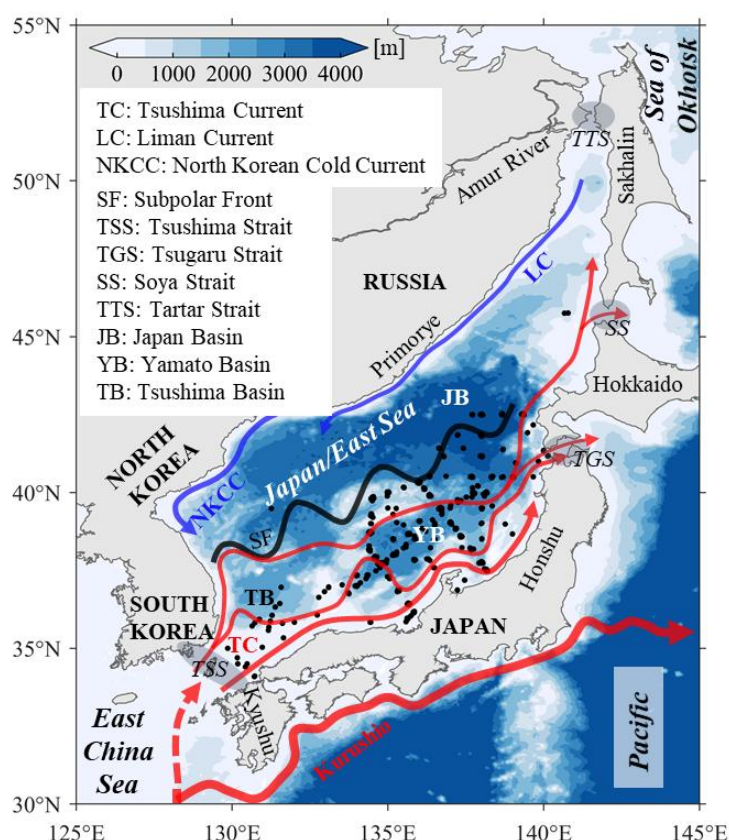
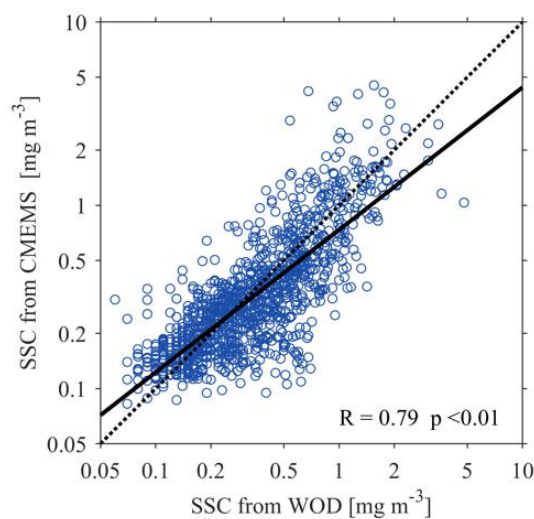
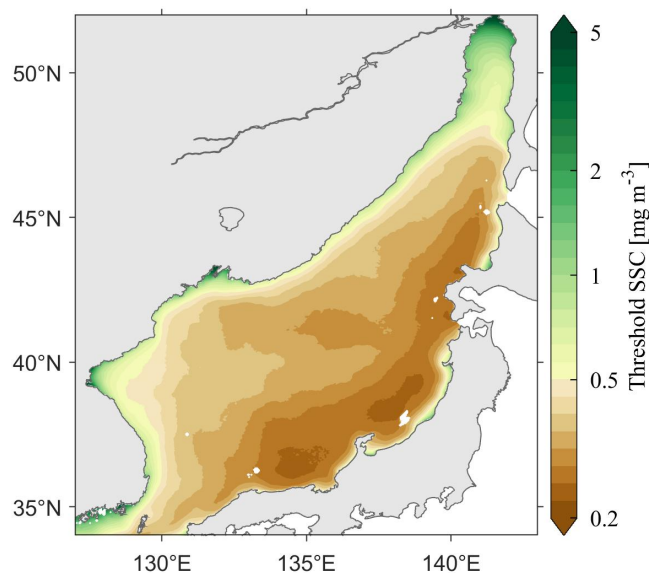


Figure 1. Topography of the JES. Red/blue arrows represent warm/cold currents (Yabe et al., 2021). Black dots indicate the *in-situ* observation stations of chlorophyll-a concentration, as derived from the WOD18.



565

566 **Figure 2. Regression between the *in-situ* observed chlorophyll-a concentrations from WOD18 (x-axis) and satellite-**
 567 **derived (y-axis) sea surface chlorophyll-a concentrations (SSCs).**



568

569 **Figure 3. Distribution of threshold SSC for a bloom at each grid in the JES over 1998–2019.**

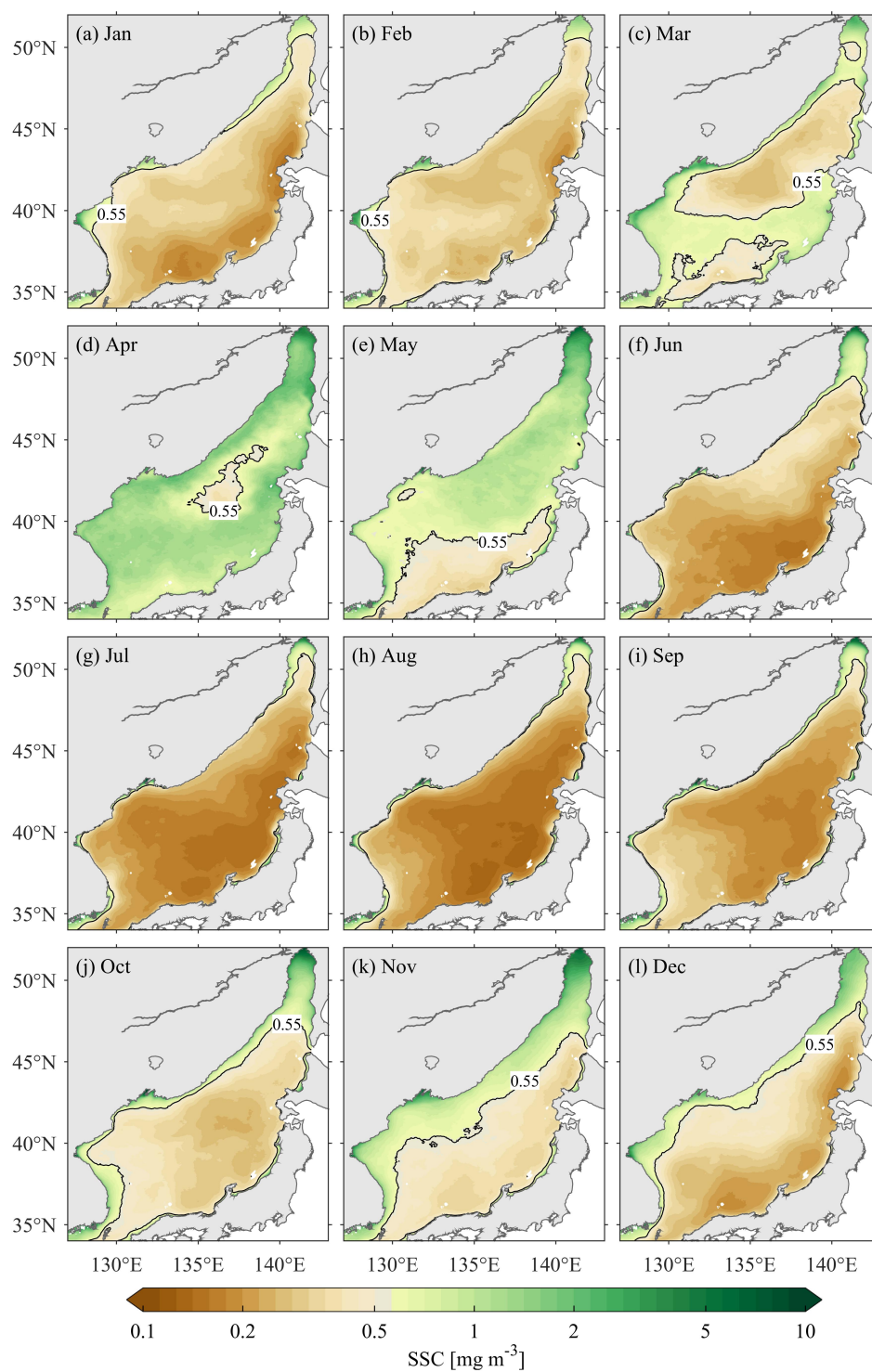




Figure 4. Distribution of climatological monthly mean SSC in the JES over 1998–2019. The black contours indicate the threshold criterion used to identify SSC blooms for the entire JES.

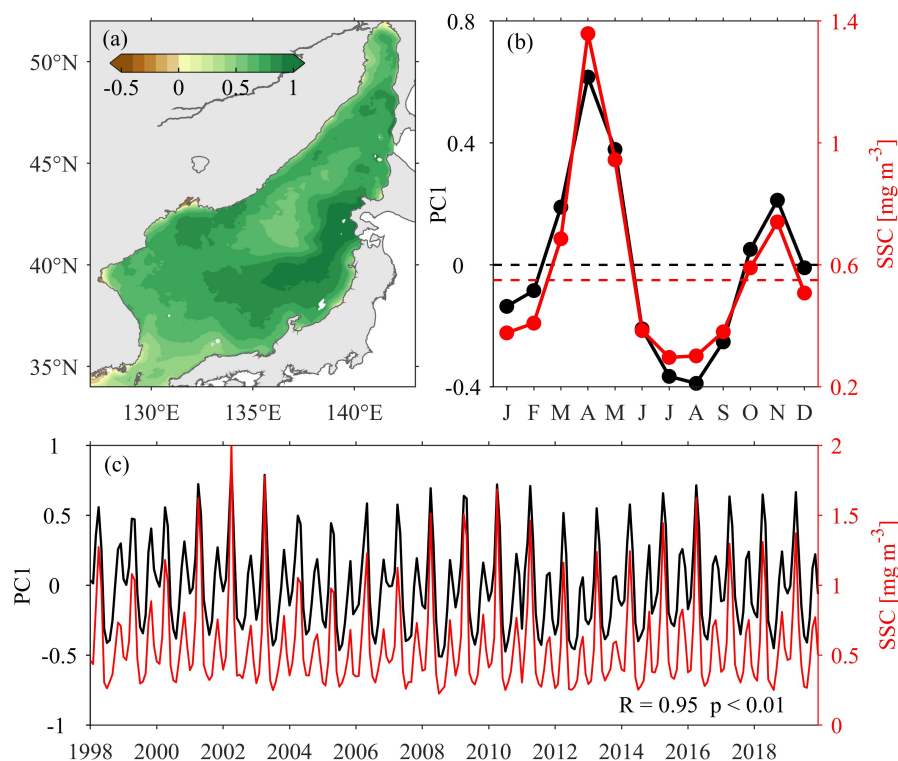


Figure 5. EOF analysis of the monthly mean SSC in the JES: (a) spatial pattern of the first EOF mode, (b) climatological and (c) monthly time coefficients (black lines). The red lines in (b) and (c) represent climatological and monthly mean area-averaged SSC values in the JES, respectively. In (b), the black dash line indicates the zero, while the red dashed line indicates the threshold criteria (0.55 mg m⁻³) of SSC blooms for the entire JES, respectively.

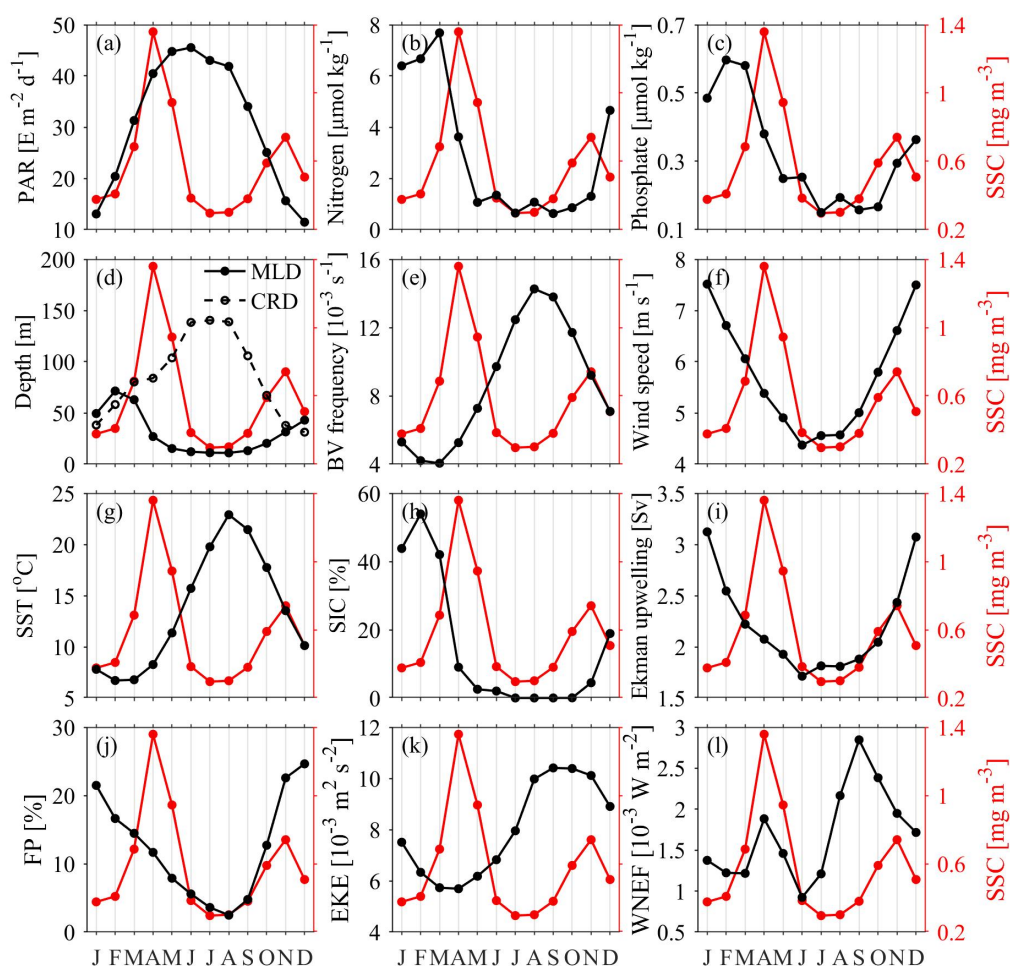
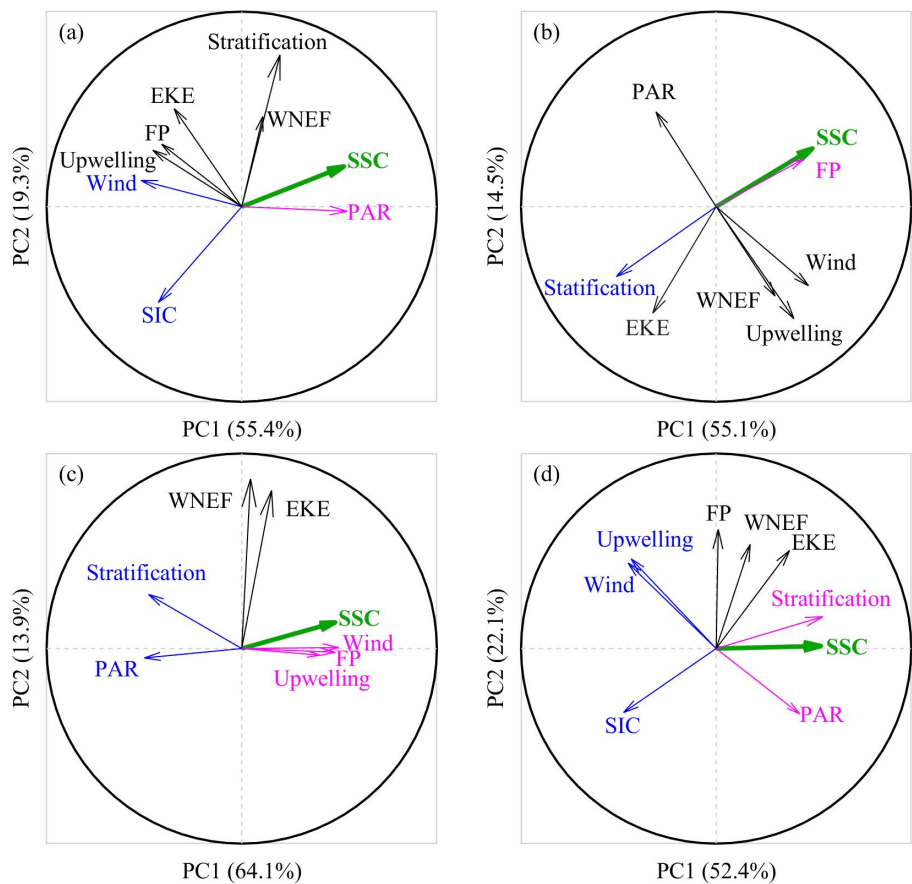
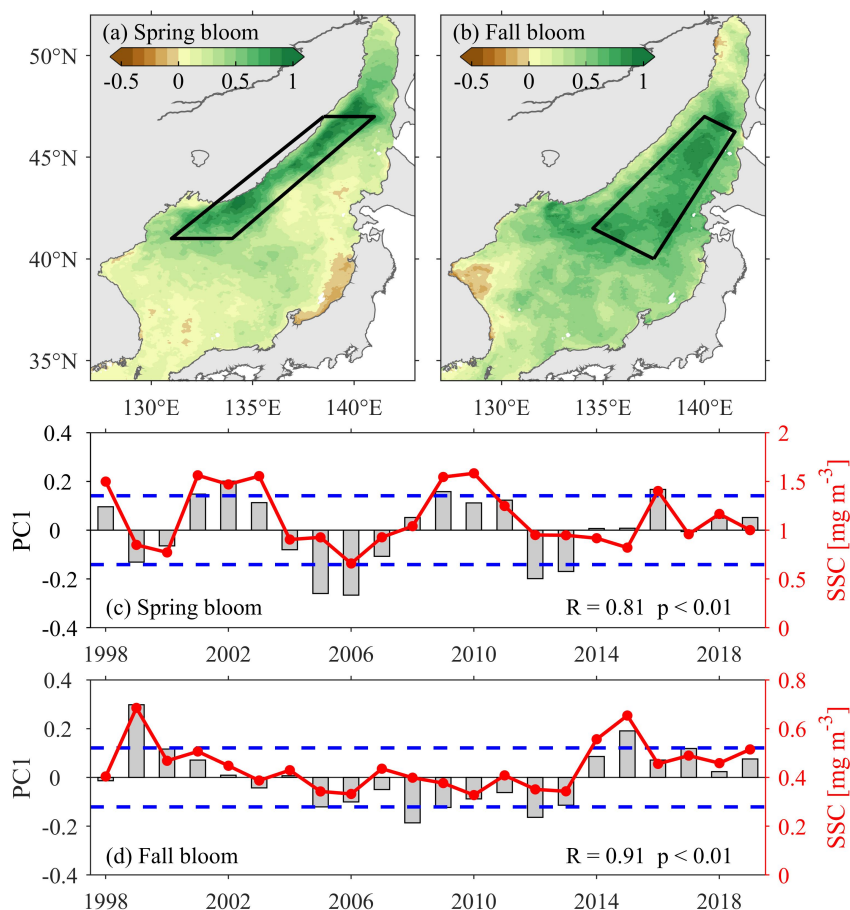


Figure 6. Climatological monthly mean series of area-averaged physical environmental factors (black lines) and area-averaged SSCs (red line): (a) photosynthetically active radiation (PAR); (b) nitrogen; (c) phosphate; (d) mixed layer depth (MLD; solid line) and critical depth (dashed line); (e) Brunt Väisälä (BV) frequency; (f) wind speed; (g) sea surface temperature (SST); (h) sea ice concentration (SIC); (i) frontal probability (FP); (j) Ekman upwelling transport; (k) wind-induced near-inertial energy flux (WNEF); and (l) eddy kinetic energy (EKE).



584
585 **Figure 7. PCA analysis of physical environmental factors (arrows) during different SSC evolution stages: (a) raise**
586 **(January–April) and (b) decline (April–July) stages of spring blooms; (c) raise (July–November) and (d) decline**
587 **(November–January) stages of fall blooms. The x- and y-axes represent the first and second principal components (PC1**
588 **and PC2), with their variance contributions marked as percentages in brackets of the x- and y-labels respectively. Arrows**
589 **close to each other denote that the corresponding factors are positively correlated, whereas those are symmetrically**
590 **opposed to each other suggest they are negatively correlated. Orthogonal arrows mean they are not correlated with each**
591 **other. The projections of the arrows on the x- and y-axes indicate the extent to which the factors are explained by PC1**
592 **and PC2, respectively. The factors positively (negatively) correlated with SSC (green thick arrows) are highlighted with**
593 **purple (blue) arrows.**



594

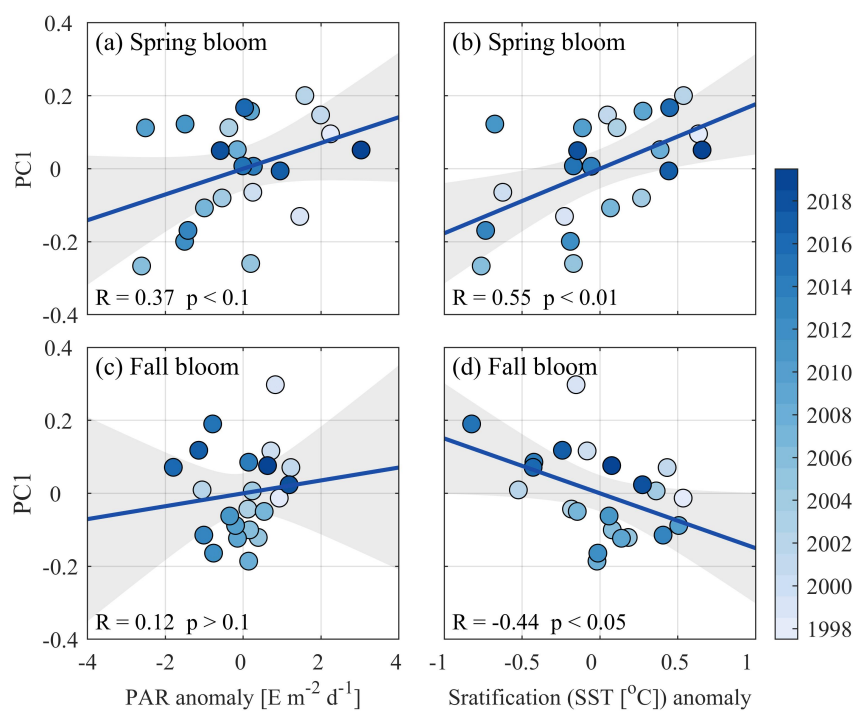
595

596

597

598

Figure 8. EOF analysis of SSC anomalies in the JES. Spatial patterns of the first EOF mode (EOF1) during (a) spring (March–May) and (b) fall (October–November). The corresponding time coefficients (grey bars) of EOF1 with standard deviation (blue dash lines), and area-averaged SSC (red lines) during (c) spring and (d) fall. The areas averaged are marked with black boxes in (a) and (b), respectively.



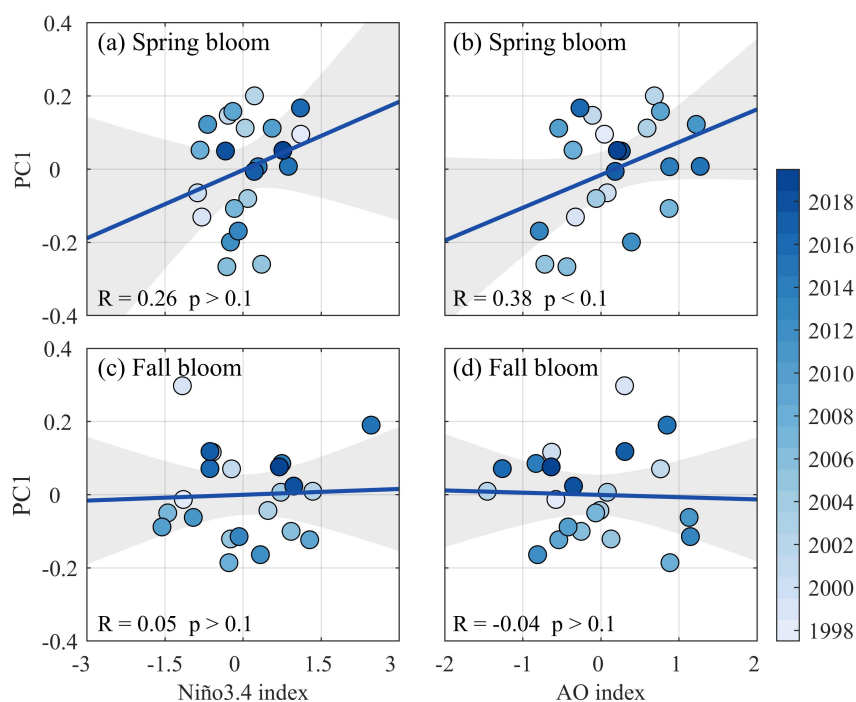
599

600

601

602

Figure 9. Scatterplots (colored dots) and linear fitting (blue lines) between PAR anomalies and PC1 in (a) spring and (c) fall and between stratification anomalies and PC1 in (b) spring and (d) fall. The gray shading indicates the 95% two-sided confidence bounds.



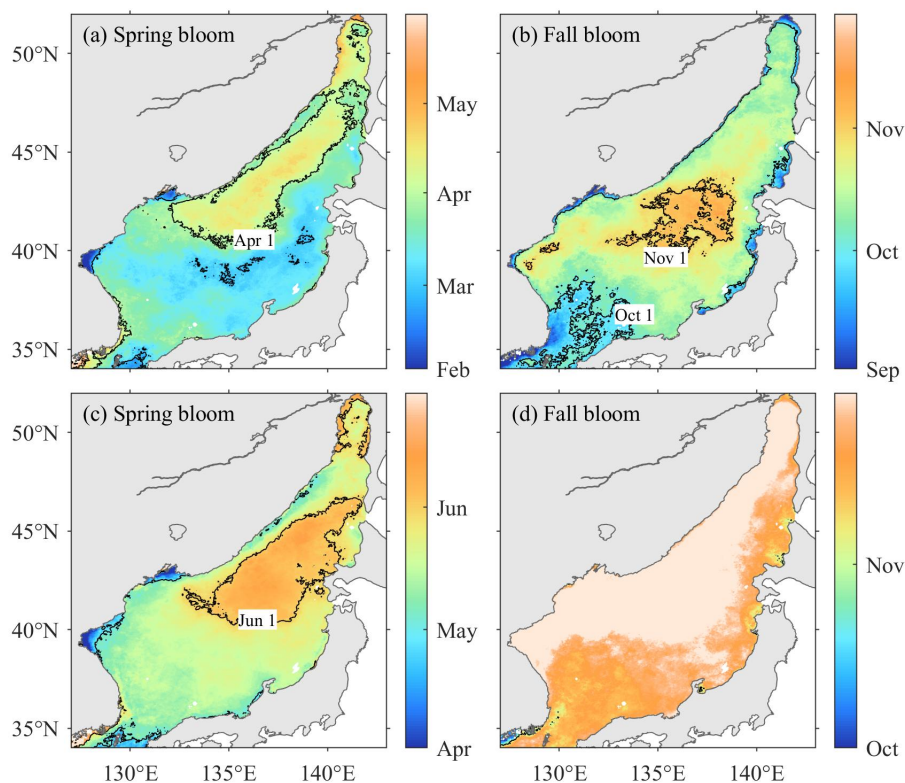
603

604

605

606

Figure 10. Scatterplots (colored dots) and linear fitting (blue lines) between Niño 3.4 index and PC1 in (a) spring and (c) fall and between AO index and PC1 in (b) spring and (d) fall. The gray shading indicates the 95% two-sided confidence bounds.

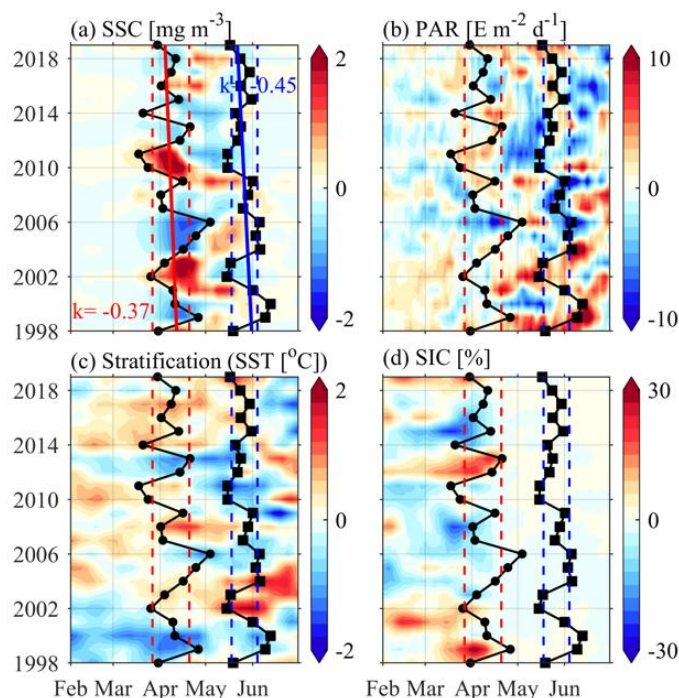


607

608

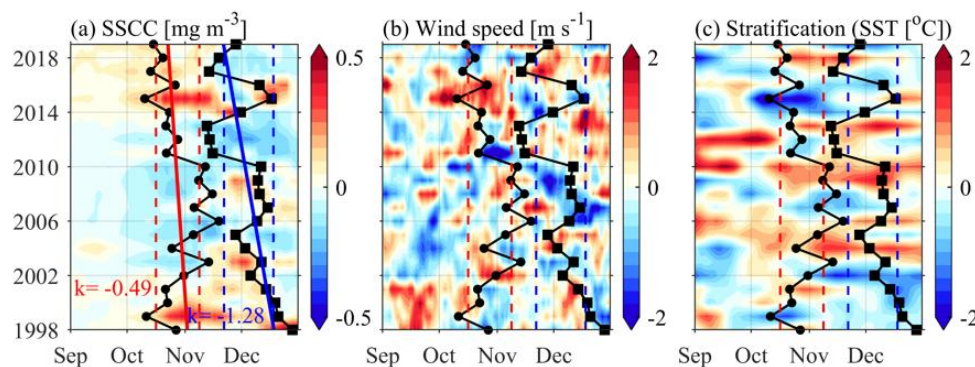
609

Figure 11. The climatological distributions of the initiation timing of (a) spring and (b) fall blooms; and the termination timing of (c) spring and (d) fall blooms. The interval between black contours is one month.



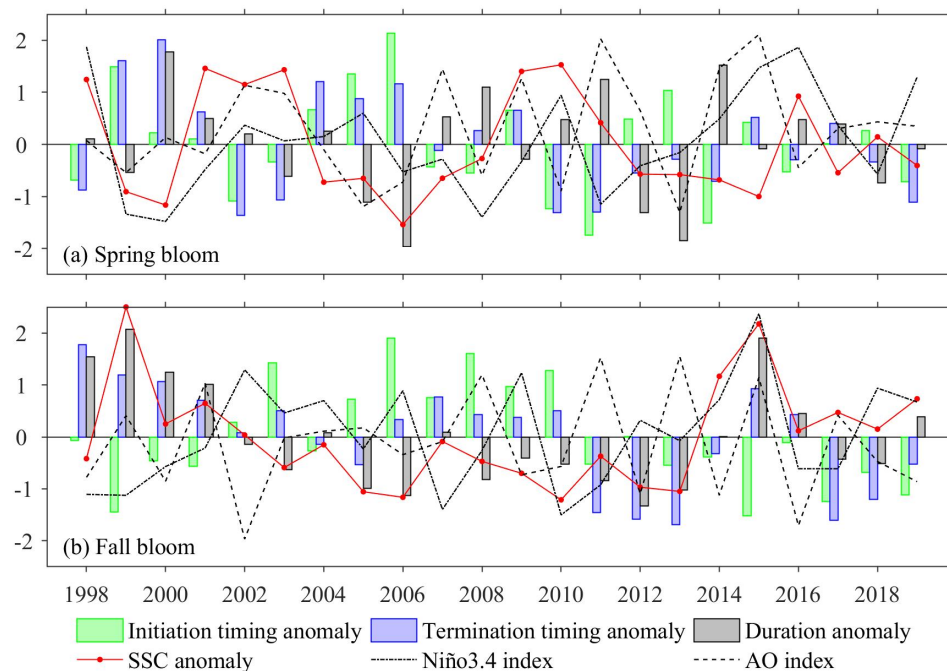
610

611 Figure 12. (a) SSC, (b) PAR, (c) stratification, and (d) SIC anomalies averaged along the JES's northwestern coast
612 (marked by the black box in Fig. 8a) from 1998 to 2019. The spring bloom initiation and termination timing are
613 represented by solid dots and square lines, with the solid red/blue lines indicating the linear trends, and the dashed
614 red/blue lines indicating the one standard deviation beyond the climatological mean initiation/termination timing,
615 respectively.



616

617 Figure 13. (a) SSC, (b) PAR, and (c) stratification anomalies averaged in the deep Japan Basin (marked by the black box
618 in Fig. 8b) from 1998 to 2019. The fall bloom initiation/termination timing are represented by solid dots/square lines, with
619 the solid red/blue lines indicating the linear trends, and the dashed red/blue lines indicating the one standard deviation
620 beyond the climatological mean initiation/termination timing, respectively.



621

622

623

624

625

Figure 14. Time series of initiation timing anomalies (green bars), termination timing anomalies (blue bars), duration anomalies (gray bars), area averaged SSC anomalies (red lines), Niño 3.4 index and AO index for (a) spring, and (b) fall blooms. The averaged areas are marked by black box in Fig. 8a and 8b for spring and fall blooms, respectively. The time series of all variables are normalized, i.e., divided by their corresponding standard deviations (STD).